Composites Part C: Open Access 20 (2026) 100741

Contents lists available at ScienceDirect

Composites Part C: Open Access

journal homepage: www.elsevier.com/locate/composites-part-c-open-access

Effect of biosourced silica nanofiller content on deformation-induced cell morphology and compression fatigue of EVA-based cellular composites

C. Aimar [a,b], R. Bordage [a], D. Ferré Sentis [b], L. Bailly [a], S. Rolland du Roscoat [a], A. Kayum [b], L. Orgéas [a,*]

[a] Univ. Grenoble Alpes, CNRS, Grenoble INP, 3SR Lab, Grenoble, 38000, France
[b] Decathlon SA - Footwear Industrial Community, Wattrelos, 59150, France

ARTICLE INFO

Keywords:
Cellular composites
Biosourced nanofillers
Compression fatigue
X-ray tomography

ABSTRACT

Closed-cell ethylene–vinyl acetate (EVA) foams reinforced with particulate fillers can be regarded as lightweight cellular polymer composites, widely used in energy-absorbing applications where compression fatigue resistance and shape recovery are critical. Although particulate fillers are commonly introduced to enhance mechanical properties, their influence on fatigue behavior through deformation-induced microstructural changes remains insufficiently understood.

In this study, the effect of biosourced silica content on the compression fatigue behavior of closed-cell EVA foams is investigated. EVA foams containing 0 to 20 wt% biosourced silica particles are manufactured while maintaining practically constant porosity (0.80) and density (0.18 g cm^{-3}), allowing the intrinsic effect of filler content to be isolated. The mechanical response under cyclic compression fatigue is correlated with post-deformation microstructural observations using scanning electron microscopy and X-ray microtomography.

The results show that increasing filler content from 0 to 20 wt% enhances initial stress levels and absorbed energies by a factor of ≈ 2, but increases both the dissipation ratio and residual strain by a factor 1.5 and 2, respectively. These trends are preserved upon cycling, with important decrease (resp. increase) of stress levels and absorbed energies (resp. dissipation ratio and residual strains) as the cycle number increases. Cyclic compression induces pronounced filler-dependent changes in cell wall morphology, including bending, buckling and localized damage leading to measurable changes in plastic strain accumulation: after cycling and strain recovery, the compression plastic strain rises from 0 to 0.15 when the filler content varies from 0 to 20 wt%. These deformation-induced morphological features provide insight into the mechanisms governing fatigue degradation and reveal a trade-off between mechanical reinforcement and fatigue durability using 10 wt% of biosourced silica.

Overall, this work demonstrates that biosourced silica content governs the compression fatigue performance of EVA-based cellular composites primarily through its influence on the evolution of deformation-induced cell wall morphology. The present results provide mechanistic understanding and practical guidance for the microstructural design of lightweight and durable cellular composite materials.

1. Introduction

Closed-cell foams made of ethylene–vinyl acetate copolymer (EVA) are extensively employed in energy-absorbing applications, and in particular in running shoe midsoles, due to their low density, resilience and ability to dissipate mechanical energy under compressive loading [1–6]. In such applications, performance often results from a compromise between lightweight, cushioning efficiency, shape recovery and durability under repeated deformation. Improving fatigue resistance while maintaining high specific characteristics therefore remains a key challenge in the design of EVA foams.

Among design strategies, the incorporation of particulate fillers is commonly employed to modify the mechanical response of the cell wall elastomers such as EVA [7]. Adding fillers is known to reinforce EVA, to modify dissipation, to influence foaming processes and thus the resulting cellular structure, thereby affecting both initial properties and long-term mechanical behavior [8,9]. For example, Chang et al. [10] recently succeeded in tuning the mechanical properties of EVA foams by

* Corresponding author.
E-mail address: laurent.orgeas@3sr-grenoble.fr (L. Orgéas).

https://doi.org/10.1016/j.jcomc.2026.100741
Received 27 January 2026; Received in revised form 6 May 2026; Accepted 11 May 2026
Available online 14 May 2026
2666-6820/© 2026 The Authors. Published by Elsevier B.V. This is an open access article under the CC BY license (http://creativecommons.org/licenses/by/4.0/).

incorporating carbon nanotubes (CNTs): the EVA foam mechanical performances was improved over thousands of compression cycles, which remains limited compared with the number of cycles such foams may be subjected to (*e.g.*, around 100,000–200,000 cycles for the midsoles of running shoes). Moreover, it could be interesting to investigate the effects of other nanosized fillers, *e.g.* with more affordable and accessible fillers than CNTs. For instance, filling bulk EVA with silica nanofillers is known to improve the EVA mechanical properties while possibly altering fatigue properties such as the reduction of shape recovery upon cycling, pointing to a complex interplay between formulation and durability [11,12]. In this context, biosourced silica nanoparticles, *e.g.* derived from rice husk ash (which is an abundantly available and a renewable agricultural by-product derived from rice milling [13,14]), have been proposed as relevant sustainable alternatives to conventional manufactured fillers, offering mechanical reinforcement while reducing environmental impact at reasonable price [15].

In addition, the mechanical response of elastomeric foams is also closely associated with the evolution of their cellular architecture. While density and average cell size are commonly used descriptors, they provide only a partial description of the complex involved deformation mechanisms, in particular under long compressive fatigue up to 100,000–200,000 cycles [7]. Indeed, compression cycling induces intricate deformation of elastomeric foam cell walls, for instance inside expanded thermoplastic polyurethane foams [16], including bending/buckling and tearing. These mechanisms progressively develop during cyclic loading and contribute to irreversible deformation and damage, as also pointed out in filled EVA foams [1,17,18]. Such microstructural changes should therefore be regarded as important deformation-induced features reflecting the mechanical response at the upper scale. Despite this, most fatigue studies on filled elastomeric foams primarily rely on macroscopic mechanical indicators. Limited studies focused on quantitative correlation to post-deformation cellular morphology [1,17], especially in three dimensions [18] to unravel the link between the mechanical fatigue properties and the underlying structural damage mechanisms.

Lastly, the literature of filled EVA foams under fatigue being very scarce, in particular with a focus on the filler content effects, the successful attempts of Chang et al. [10] to improve the CNT-filled EVA foam durability under dynamic fatigue tests up to 10,000 compression cycles is of considerable interest. However, as the initial microstructure and density of the foams varied with the carbon nanotube content, identifying whether density, filler content, or induced foam microstructure that primarily control the properties specified in the foam design requirements remains complex. As a result, the way filler content alters compression fatigue performances through the evolution of deformation-induced cellular morphology remains insufficiently documented in particular for EVA foams reinforced with (biosourced) fillers.

Thus, in this work, EVA foams reinforced with biosourced silica nanoparticles (0–20 wt.%, derived from rice husk ash) are manufactured at industrial scale while strictly maintaining constant porosity, allowing the intrinsic effect of filler content to be isolated from porosity-related effects. The mechanical response under short and long-term cyclic fatigue (up to 200,000 cycles) is investigated and systematically correlated with post-compression microstructural observations using either scanning electron microscopy and X-ray microtomography. Particular attention is paid to the evolution of cell wall morphology induced by cyclic compression. Doing so, the objective of this study is to elucidate how filler content controls the evolution of deformation-induced cellular morphology and how this evolution, in turn, affects compression fatigue performance and shape recovery in biosourced silica-reinforced EVA foams. By linking formulation, microstructural evolution and macroscopic response, this work provides mechanistic insight into fatigue-induced degradation mechanisms and contributes to the rational design of sustainable lightweight EVA foams for energy-absorbing applications.

2. Materials and methods

2.1. Raw materials and foam processing

The studied ethylene-vinyl acetate copolymer (EVA) formulation consisted in 91 wt.% of EVA (VA content ≈ 22 wt.% and PE content ≈ 78 wt.%) and 9 wt.% of other additives: blowing agent (azodicarboxamide), blowing agent activator (zinc oxide), initiator (dicumyl peroxide) and pigment (titanium oxide). This formulation is commonly employed for running shoe midsoles [6]. Instead of using conventional (in)organic fillers, we used biosourced nanofillers, *i.e.*, rice husk ashes under the form of white precipitated amorphous silica [19] with a mean diameter of the particles smaller than 40 nm. Five grades were produced with 0 wt.%, 5 wt.%, 10 wt.%, 15 wt.%, and 20 wt.% of biosourced silica nanofillers.

To process the foams, the EVA blend was first mixed with pigments and nanofillers in a Kneader machine at 125 °C. The blowing agent, activator and initiator were then added at 105 °C. The mixture was blended in a calendering machine at 60 °C before entering a pelletizer which produced pellets of typical size ≈ 1 cm. Foams were then obtained using injection molding with a targeted porosity $\phi = 0.8$ whatever the considered grade. To conform to this specification together with the decrease of the melt flow index with the amount of fillers [20], the amount of blowing agent was adjusted for each grade (*e.g.,* the blowing agent content varying from 5.3 to 6.7 wt.% for the foams with 0 to 20 wt.% of nanofillers, whereas the amount of initiator was slightly excessive in the basic formula, so none was added). Once produced, foam slabs (typical dimensions: $1 \times 14.7 \times 24.5$ cm^3) were obtained when opening the mold (mold dimension: $0.6 \times 9.2 \times 15.3$ cm^3). We removed (with a slicer) the 2 mm outer surface of the foam slab. The foam slab density was then determined by measuring both its mass (with a high precision scale, precision: 0.1 mg) and volume (with a high precision caliper, precision: 0.01 mm). Samples (cylinders with 2 mm diameter and 2 mm height) were extracted from it and air-conditioned prior to testing, *i.e.*, for compression fatigue and imaging (55% RH and 23 °C).

2.2. Cyclic compression

Foam cylindrical samples were subjected to cyclic compression tests along their vertical axis (further noted $\mathbf{e}_z$) using a standard electromechanical testing machine (Instron n.5994, 10 N load cell). During the tests, the nominal compression stress σ and the compression Hencky strain ε were derived from the measured axial force and displacement of the cross-head, respectively. Mechanical fatigue tests consisted in $N = 200,000$ cycles of load-unload compression at 1.25 Hz with a maximum compression strain $\varepsilon^{max} = 1.6$. This cyclic loading roughly corresponds to 400 to 700 km ran [6,18]. The test was repeated on three different samples of each grade. As reported previously [6,18], several properties were monitored over the N cycles of each foam: the maximum stress σ^{max}, the absorbed volumetric energy W_{abs} and its maximum value W_{abs}^{max} during loading, the maximum volumetric dissipated energy per cycle W_{diss}^{max}, the dissipation ratio $\eta = W_{diss}^{max}/\pi W_{abs}^{max}$, the residual strain ε^{res} right after the end of the cyclic tests. The recovery of each sample was also monitored at $t = 1$ min, 1 h, 24 h, 1 week, 1 month and 3 months after the end of the fatigue test, by assessing the time evolution of the compression residual strain ε^{res}.

2.3. Structural characterization

2D microstructural characterization and chemical analysis – Scanning electron microscopy (SEM; Zeiss Ultra55) was used to get micrographs of the cross sections (covered by a 10 nm carbon film) of undeformed samples to observe the cellular structures of the foams and the phase distribution in the cell walls. Similarly, SEM micrographs were also acquired one month after the cyclic tests to analyze fatigue-induced

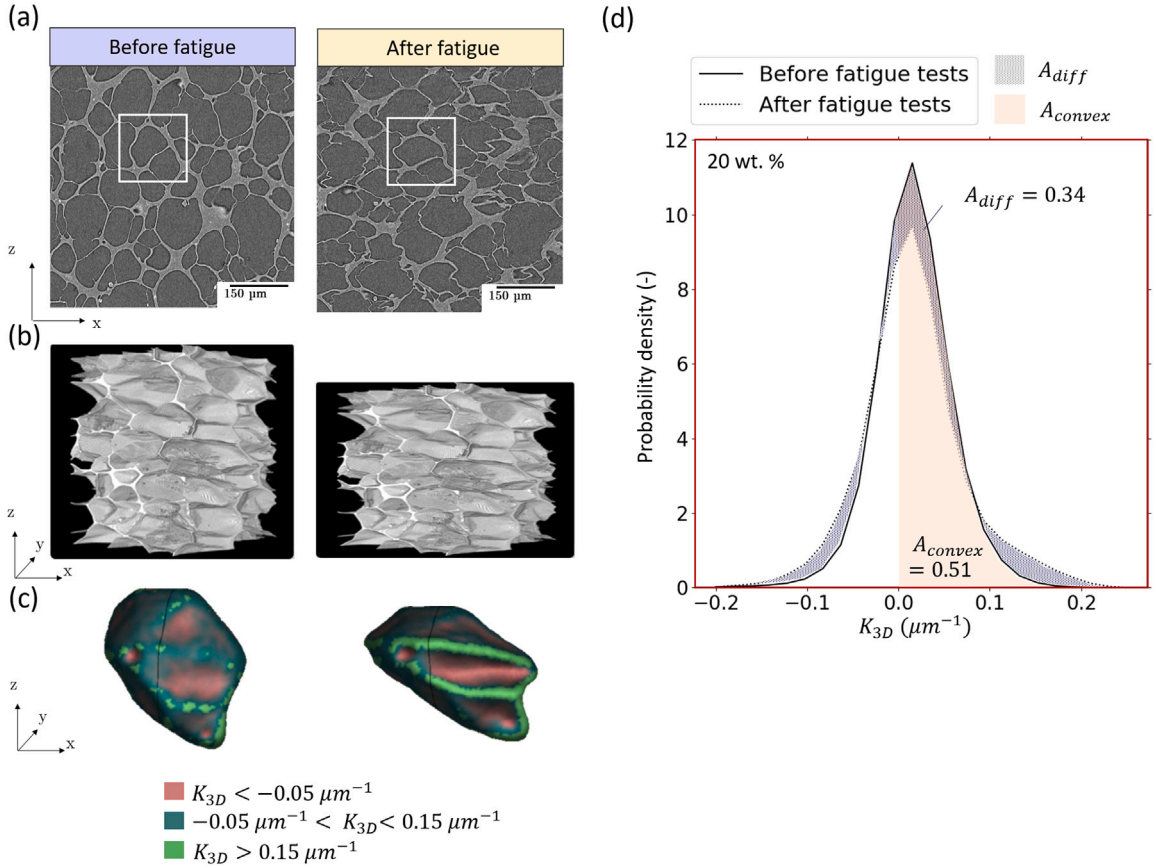

Fig. 1. (a) 2D grayscale slices and (b) 3D views of the same Region Of Interest (ROI) of sample with 20 wt.% of nanofillers before (left) and one day after (right) fatigue obtained by X-ray tomography after registration in which the same cell is framed in white. (c) 3D representation of the cell selected in (a) before (left) and one day after (right) fatigue and its associated mean curvature map (highly concave surface in red, highly convex surface in green). (d) 3D mean curvature κ_{3D} distributions, before and one day after fatigue tests, of 100 cells of the 20 wt.% nanofilled foam, illustrating the convex area A_{convex} (convex area fraction) and the area of the difference between both distributions A_{diff} of its cell walls.

damage. SEM energy dispersive X-ray (EDX) mode was also used to get local chemical composition of the foam components, in particular to distinguish the different mineral fillers.

3D cellular morphology – 3D images of the same samples were obtained using X-ray microtomography before and one day after fatigue tests as shown in Fig. 1a and b, following the procedure described in previous studies [18]. Tomographic acquisitions were performed using a RX Solutions system equipped with a Hamamatsu Photonics source LaB_6 cathode (acceleration voltage: 60 keV, current: 7 µA, frame rate: 1 s^{-1}, projections: 2400, voxel size: 1 μm^3). Therewith:

- We estimated the mean residual Hencky strains components ϵ_{xx}, ϵ_{yy}, ϵ_{zz} as well as the mean residual volumetric strain ϵ_{vol} one day after fatigue tests by analyzing the 3D grayscale images with Digital Volume Correlation (DVC) implemented in the software SPAM [21].
- The 3D images were segmented using Weka plugin of the software Fiji [22,23]. The resulting binarized images were then used to estimate key structural descriptors using the Analyze3D and BoneJ plugins of Fiji [24,25]: the porosity ϕ, the mean wall thickness t, the mean cell size d and the foam degree of anisotropy DA (for isotropic porous media $DA = 0$, and for highly aligned porous media $DA = 1$) together with the orthogonal directors $\mathbf{e}_I, \mathbf{e}_{II}, \mathbf{e}_{III}$ of this anisotropy.
- Using the method reported in [18], we also computed (from the 3D segmented images) the number of the foam closed pores N_p. This metric was used to quantify the formation of fatigue-induced damages in cell walls (tears, holes), which are directly related to a decrease of N_p.
- Plastic cell wall bending/buckling is also prone to occur during cyclic compression [18,26]. To our knowledge, no method had yet been developed to quantify these defects. To address this, we proposed a three steps procedure using segmented and grayscale images and Fiji : (i) cell labelization, (ii) wall surface detection and (iii) 3D mean curvature computation. The cell labelization was based on a marching cubes algorithm [24]. The center of inertia of each labeled cells was then used to start a first coarse wall detection of each cell using a "surfels" generation and expansion with Limeseg plugin of Fiji [27] (with parameters set as follows: $d_0 = 5$ to 1, $f_{\text{pressure}} = 0.1$, $Z_{\text{scale}} = 1$, range in d_0 units $= 2$, number of iteration steps $= -1$, and $RealXYPixelSize = 1$). Refinements were made by progressively decreasing the surfel diameter d_0 to improve the accuracy of the surface detection. Once the surface/wall of each cell was fully detected, the local mean 3D curvature κ_{3D} was calculated using a least squares method on the surface (Fig. 1c). For each grade, local values of κ_{3D} were estimated using at least the surfaces of 100 cells before and after fatigue. The probability density function of κ_{3D} was then obtained (Fig. 1d). Since each cell initially exhibits both concave and convex surfaces, the initial fraction of convex surfaces A_{convex}, defined as the proportion of surface points with $\kappa_{3D} > 0$, was calculated to describe the initial wall shape (Fig. 1d). Moreover, we also computed the difference between the curvature distributions before and after fatigue, noted as A_{diff} (Fig. 1d). This metric is an indicator of structural change: the higher the A_{diff} value, the stronger the cell wall bending/buckling induced after fatigue.

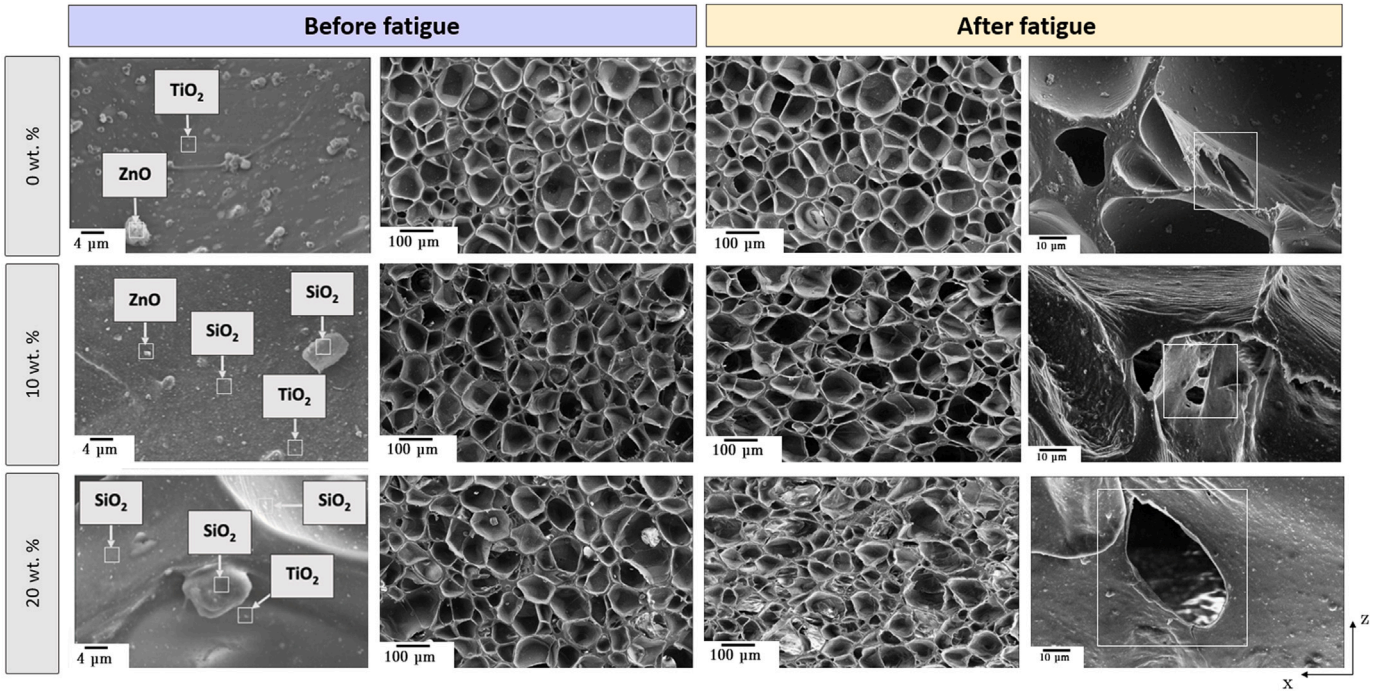

Fig. 2. SEM micrographs of some typical produced foams with 0, 10 and 20 wt.% nanofiller content in the *zx* plane, showing (i) the presence of SiO_2 nanoparticles inside cell wall as well as micro and nano-sized particles and aggregates on the surface of cell walls, (ii) the morphology of cells and cell walls before (left) and one month after (right) compression fatigue.

Table 1
Structural descriptors of produced foams filled with increasing amount of silica nanofillers.

Parameters	0 wt.%	5 wt.%	10 wt.%	15 wt.%	20 wt.%
ρ (g cm^{-3})	0.17 ± 0.02	0.17 ± 0.02	0.18 ± 0.02	0.17 ± 0.02	0.18 ± 0.02
ϕ	0.80 ± 0.01	0.79 ± 0.01	0.79 ± 0.01	0.80 ± 0.01	0.79 ± 0.01
d (µm)	48 ± 23	61 ± 26	59 ± 25	60 ± 26	59 ± 28
t (µm)	9.3 ± 5.1	12.8 ± 8.4	12.7 ± 7.9	11.8 ± 6.8	11.9 ± 5.9
DA	0.14	0.13	0.13	0.11	0.15
N_p (mm^{-3})	2261	2695	3114	3100	4036
A_{convex}	0.66	0.63	0.53	0.53	0.51

3. Results and discussion

3.1. Initial foam structures

Results reported in Table 1, Figs. 2 and 3 give some interesting information about the architectures of foams and the microstructures of cell walls before mechanical cycling:

- As shown in Table 1, the porosity ϕ estimated from the 3D images ranges between 0.79 and 0.80 whatever the considered nanofiller content: the processing route we used indeed conducted to practically constant sample porosity. It is also interesting to note that whatever the nanofiller content, the foam density ρ lies between 0.17 g cm^{-3} and 0.18 g cm^{-3}, which is in agreement with typical value of polymeric foams used in athletic running shoes, *i.e.*, from ρ = 0.09 g cm^{-3} to ρ = 0.3 g cm^{-3} [1,2,26,28]. Thus, the trends we report and discuss hereafter about the foam mechanical properties are identical to those we would establish for the specific mechanical properties in a context of design of lightweight materials.
- Regardless of the nanofiller content, the cellular architectures exhibit very close features, with a mean cell size $d \approx 57$ µm and a mean wall thickness $t \approx 12$ µm (Table 1). These values are in agreement with those reported in previous studies for similar

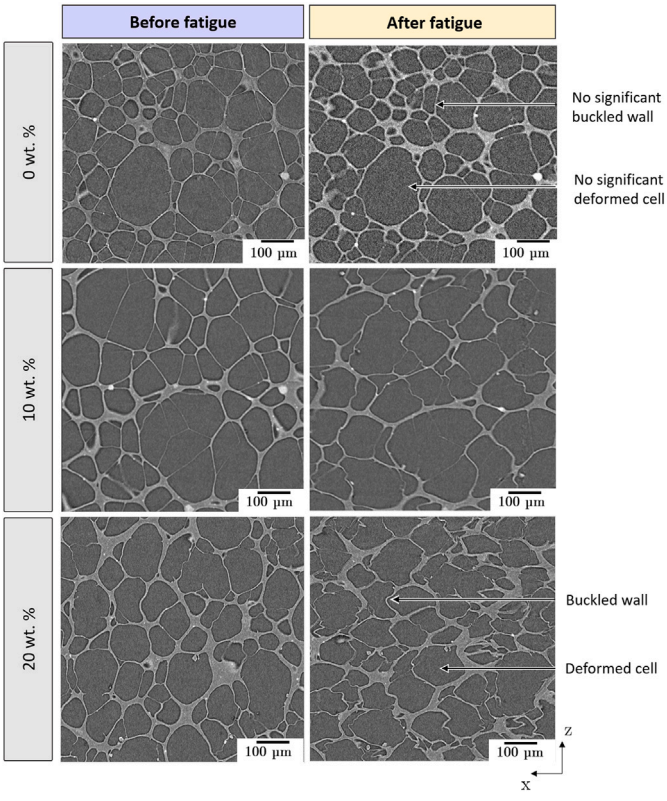

Fig. 3. 2D grayscale *zx* slices (X-ray tomography) of the same ROIs before (left) and one day after (right) compression fatigue along the *z* direction, for three typical produced foams with 0, 10 and 20 wt.% nanofiller contents.

foams [6,18]. However, foams containing nanofillers display a slight increase in cell size and cell wall thickness. This increase can be explained by the competition between (i) the increase in nucleation sites as the nanofiller content increases, promoting the decrease in cell size [29], (ii) the rise of the viscosity material with the nanofiller content [20], together with (iii) an increase in the time between the blowing and the gelling of the foam [30]. The two last points promoting the cell size increase [20] and are presumably predominant in the produced nanofilled foams.

- The foam cellular structures also present a small and quasi constant degree of anisotropy $DA \approx 0.13$, which proves that the produced cell architectures exhibit a weak transverse isotropy with a minor direction $\mathbf{e}_{III}$ parallel to the slab thickness and the compression axis $\mathbf{e}_z$ (Table 1). Such a low value is probably driven by the injection molding process we used. It is very different from what was reported for EVA foams processed by compression molding, which exhibited marked in-plane anisotropy (DA of 0.4, [18]).
- The inspection of the SEM micrographs (Fig. 2) as well as the acquired 3D images (Fig. 1) proves that the initial foam architectures mainly display closed cells. Furthermore, as reported in Table 1, an increasing number of pores N_p with the nanofiller content is observed. This trend is difficult to interpret in absolute values because the very thin walls that are more present in the foam without or with low nanofillers remain challenging to detect with the considered spatial resolution.
- Values given in Table 1 also show a slight decrease of A_{convex} with the nanofiller content, emphasizing a weak increase of the cell wall bending induced during the foaming process. This trend is illustrated in the 2D slices reported on the left side of Fig. 3. Such weak cell wall bendings may be related to possible elastic confinement stresses induced by the denser skin of the produced slabs during demolding, which conducted in slight buckling of some cell wall inside the slabs.
- Fine scale SEM observations reported in Fig. 2 show the presence of some micro and nanosized fillers of zinc and titanium oxides even for the foam without biosourced silica nanofillers. As mentioned in the previous section, these particles are added in commercial foams used in the running shoes midsoles [1]. In addition, for foams filled with biosourced particles, the SEM EDX analyses confirmed the incorporation of SiO_2 nanoparticles inside the polymer matrix. Moreover, while increasing the nanofiller content, a small but increasing number of SiO_2 aggregates with average dimension 1–5 μm were observed on the surface of cell walls, emphasizing some difficulties to properly disperse SiO_2 nanoparticles during the mixing step.

3.2. Mechanical properties upon cycling

3.2.1. First cycle

The stress–strain curves reported in Fig. 4a for the first compression cycle resemble most of stress–strain responses of elastomeric foams [6,18,31,32] with (i) three typical deformation regimes mainly ascribed to the foam architectures and cell wall deformation modes, (ii) a nice superelastic behavior with limited dissipation ratio (Fig. 4d) and residual strain (Fig. 4e). These features are correlated to the high elasticity and the limited viscous effects of the EVA, as well as to the compression of the gas inside the cells and to plastic events such as possible decohesion and slippage at EVA-fillers interfaces [6].

In addition, the graphs reported in Fig. 4 also emphasize the important effects of the silica nanofiller content on the mechanics of EVA foams. Indeed, most of mechanical descriptors (*i.e.*, maximum stress, maximum absorbed energy and dissipation ratio) markedly increase with the nanofiller content (Fig. 4b–d). Astonishingly, the residual strain remains quite constant below 20 wt.% of nanofillers ($\varepsilon^{res} \approx 0.07$, Fig. 4e). At 20 wt.%, this deformation is, however, three times higher.

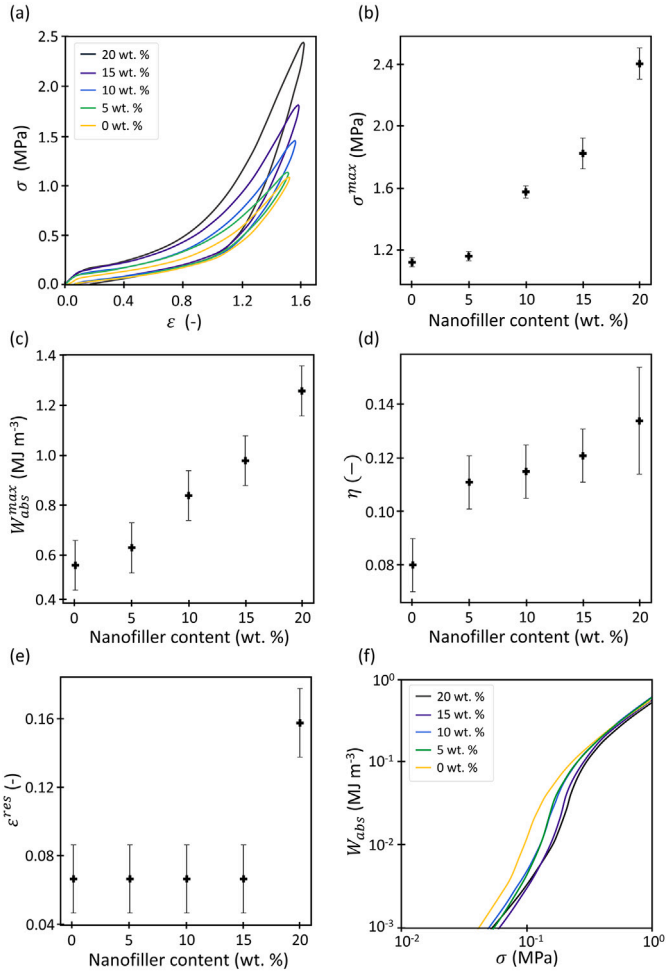

Fig. 4. Mechanical behavior of foams with 0–20 wt.% nanofillers during the first compression cycle ($N = 1$) for the 5 studied nanofiller contents: (a) stress–strain curves; maximum stress (b) and maximum absorbed volumetric energy (c), dissipation ratio (d) and residual strain (e) as functions of the nanofiller content; (f) volumetric absorbed energies as function of the compression stress upon loading. Errors bars stand for the standard deviation.

Lastly, by following concepts proposed in [32], *i.e.*, a proper cushioning material should maximize the absorbed energy while minimizing compressive stress upon loading, the graph reported in Fig. 4f proves that the higher the nanofiller content, the poorer the foam cushioning capability during the first cycle. This is probably due to the slight difference observed regarding the initial bent cell walls, since a small decrease of A_{convex} is noticed as the nanofiller content increases (Table 1): the less the initial bent shape of cell walls, the higher the energy to buckle them is required and the higher the cushioning capability. Apart from this effect, the well-known reinforcement effects of the elastomeric walls with a higher filler content [15] is more likely to be responsible for the observed foam mechanical properties than the weak structural differences between the samples with and without nanofillers presented in Table 1.

3.2.2. Effect of cycling

The graphs plotted in Fig. 5 give the mechanical descriptors σ^{max}, W_{abs}^{max}, ε^{res} and η with the cycle number N. It is worth noting that the general trends observed in these graphs are in good agreement with those reported in the literature for similar elastomeric foams [6,18]: marked decrease (resp. increase) of σ^{max}, W_{abs}^{max} and η (resp. ε^{res}), with simultaneously both a bell-shape evolution of η and a sharper increase of ε^{res} close to $N \approx 1000–5000$.

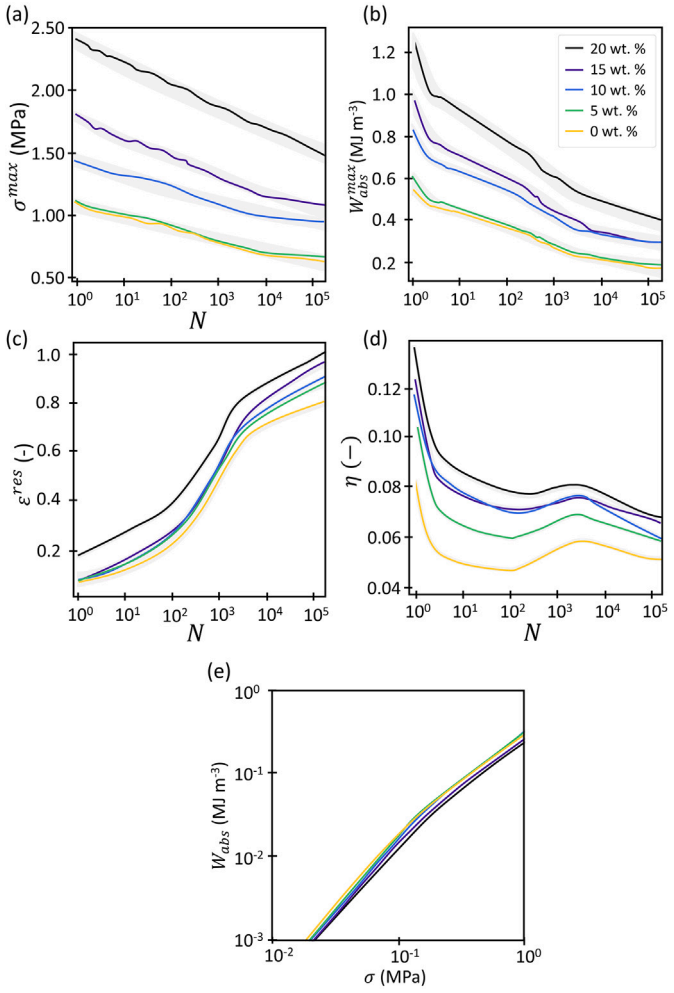

Fig. 5. Evolutions of (a) the maximum stress σ^{max}, (b) the volumetric maximum absorbed energy W_{abs}^{max}, (c) the residual strain ε^{res} and (d) the damping loss factor η with the number of cycles N for the foams with 0–20 wt.% nanofillers during compression fatigue. The gray bands illustrate the standard deviation of the measurements. Graph (e) plots the volumetric absorbed energies as function of the compression stress upon loading at $N = 200000$.

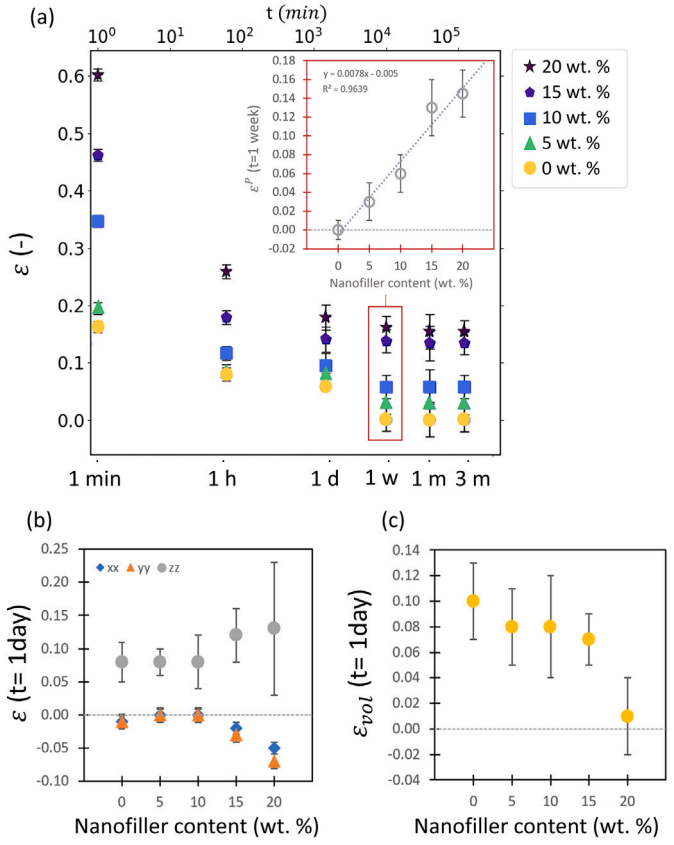

Fig. 6. (a) Evolution of the axial compression residual strain ε^{res} with the recovery time t and plastic strain ε^{p} (after $t = 1$ week of recovery) as a function of nanofiller content (inset). Graphs (b) and (c) gives the components of the Hencky residual strain tensor (b) and Hencky residual volumetric strain (c) in the fatigued samples, as estimated from the 3D images and DVC after 1 day of recovery time. Errors bars illustrate the standard deviation.

Furthermore, the effects of the nanofiller content is clearly highlighted. Firstly, the trends we emphasized for the first cycle (Fig. 4) are still preserved, *i.e.*, the higher the nanofiller content, the higher the maximum stress, the maximum absorbed energy, the residual strain, the dissipation ratio and the lower the cushioning capability, whatever the considered cycle N. Secondly, graphs of Fig. 5a and b show a marked decrease of the mechanical properties such as σ^{max} and W_{abs}^{max} with N, these tendencies being accompanied by a marked increase in the residual strain ε^{res}. Thirdly, the rate magnitude of the aforementioned trends is higher for higher nanofiller content. These two important observations are presumably related to cell scale structural damage or plastic deformation (see next subsection), which should in turn be linked with possible microscale damage or plastic mechanisms in the cell wall, *i.e.*, in the polymer and at polymer-nanofillers interfaces. Lastly, at the end of fatigue tests (*i.e.*, for $N = 200,000$), Fig. 5e shows that cycling has (i) changed the shapes of energy-stress curves, thus altering the cushioning properties of the whole foams, (ii) markedly restrained the cushioning differences between silica-filled or unfilled foams. This is related to the important residual strains: at the cell scale, these huge values should induce an important increase in the residual bent cell walls after unloading (see next section), which should thus alter possible cell wall buckling and promote cell wall re-bending upon loading, and therefore altering cushioning.

3.3. Fatigue-induced plasticity/damage

3.3.1. Foam recovery after fatigue tests

Fig. 6a shows the evolution of the compression residual strain ε^{res} as a function of recovery time after fatigue tests, the latter being varied from $t = 1$ min to $t = 3$ months. Regardless of the nanofiller content, the residual strain gradually decreases with time until it reaches a stable plastic strain ε^{p}. Whatever the considered foam, the time to end of recovery is long and may be ascribed to the viscoelasticity of the EVA coupled with diffusion (resp. flow) of the gas between the closed (resp. connected) cells [17,18]. Moreover, the higher the nanofiller content, the higher the recovery rate, so that after one day the recovery is practically over for foams with 15 wt.% and 20 wt.%, whereas longer time is needed for lower filler content, around a week.

Fig. 6a also shows that the strain recovery of the foam without silica is complete, *i.e.*, $\varepsilon^{p} \approx 0$, illustrating a "good" viscoelastic behavior. In contrast, the recovery of reinforced foams is incomplete ($\varepsilon^{p} > 0$) even after three months, highlighting the occurrence of fatigue-induced plastic events at lower scales (detailed in Section 3.3.2). Notably, the inset of Fig. 6a illustrates a linear increases of the plastic strain with the nanofiller content, with a noticeable plastic strain of 0.15 for the foams with 15 and 20 wt.% of silica nanofillers. For these two contents, the results are in line with those obtained from the 3D images and DVC: as evidenced in Fig. 6b, the residual axial strain ε_{zz} is close to ε^{p}.

Fig. 6b and c also prove that for these two contents, different plastic deformations are observed: a marked compaction $\varepsilon_{vol} \approx 0.07$ with a moderate lateral expansion $\varepsilon_{xx} \approx \varepsilon_{yy} \approx -0.025$, and a weak compaction $\varepsilon_{vol} \approx 0.01$ with an important lateral expansions $\varepsilon_{xx} \approx \varepsilon_{yy} \approx -0.075$, for filler contents of 15 wt.% and 20 wt.%, respectively. For lower filler contents, similar conclusion cannot be drawn straightforwardly from these graphs in Fig. 6b and c, since after one day their recovery has not ended (see Fig. 6a). Presumably, these samples should again exhibit a different trend, with a weak compaction ε_{vol} (from 0 to 0.06) and practically zero-valued lateral expansion $\varepsilon_{xx} \approx \varepsilon_{yy} \approx 0$.

3.3.2. Cell wall plasticity/damage

The various 2D or 3D micrographs shown in Figs. 1, 2 and 3 clearly illustrate the structural evolution of the foams before and after compression fatigue and recovery. Whatever the considered nanofiller content, two typical features are observed in cell walls: (a) some permanent bent zones (Figs. 1a–b, 3) and (b) the occurrence of tears/holes (fourth column of Fig. 2). These observations are in line with the literature [17,18]. The magnitude of these coupled plastic/damage phenomena highly depends on the silica nanofiller content and is discussed in the following points thanks to the structural descriptors introduced in the experimental section:

- Fig. 7c illustrates the evolution of A_{diff}, which gauges the increase of cell wall bending in foams after cycling and a one day recovery, as a function of the nanofiller content. Obviously, a noticeable increase of A_{diff} with the filler content is observed, from ≈ 0.12 to 0.34. The non-zero value obtained without silica nanofillers is in accordance with the micrographs shown in the first line of Fig. 3, which underlines some rare bent cell walls after compression. However, bearing in mind that without silica fillers, the sample recovery (i) is not ended after one day (Fig. 6a), (ii) processes without plasticity (Fig. 6a), these bent zones would probably disappear and A_{diff} would presumably tend to 0 after full recovery. Similarly, after full recovery, the A_{diff} values reported after one day (Fig. 7c) for 5 and 10 wt.% filler contents would probably reach lower values too.
- It is interesting to notice that fatigue-induced permanent cell wall bending mainly arises perpendicular from the compression axis, as qualitatively illustrated in the micrographs of Fig. 3. This is quantitatively supported by the structural analysis. Indeed, combined with the possible lateral plastic expansion of the fatigued samples (for 15 and 20 wt.% samples, Fig. 6b), fatigue-induced cell wall bending/buckling induces plastic anisotropy of the foams with (i) a marked increase of DA with the silica content (Fig. 7b) and (ii) invariant anisotropy directions, with a minor direction $\mathbf{e}_{III}$ which remains parallel to the compression axis after fatigue $\mathbf{e}_z$.
- As evidenced in Fig. 7a, the number of closed pores N_p after fatigue decreases while increasing the nanofiller content. This decrease is limited for the foam without silica (less than 10 %) whereas a decrease of more than 60 % is observed for a 20 wt.% of nanofiller.

Keeping in mind that the initial foam architecture displays practically identical initial features, the aforementioned fatigue-induced plastic/damage phenomena, which become more prominent as the filler content is increased, are probably ascribed to cyclic stress concentrations in the EVA around nanofillers together with the mechanics at the EVA-fillers interfaces. At the sample scale, these defects mostly explain the decrease in the maximum compression stress and absorbed energy upon cycling (Fig. 5a–b, [18,26]). Combined with viscoelastic effects, they also provide relevant causes of the residual strain growth upon cycling (Fig. 5c). In particular, cell wall tears that alter the macroscale viscoelasticity of the foams by inducing additional viscous drag forces in between new connected cells [18], would probably mainly arise around $N \approx 1000–5000$. This could explain both the sharp increase of the residual shape ε^{res} and the bell shape of the dissipation ratio η observed after such a number of cycles.

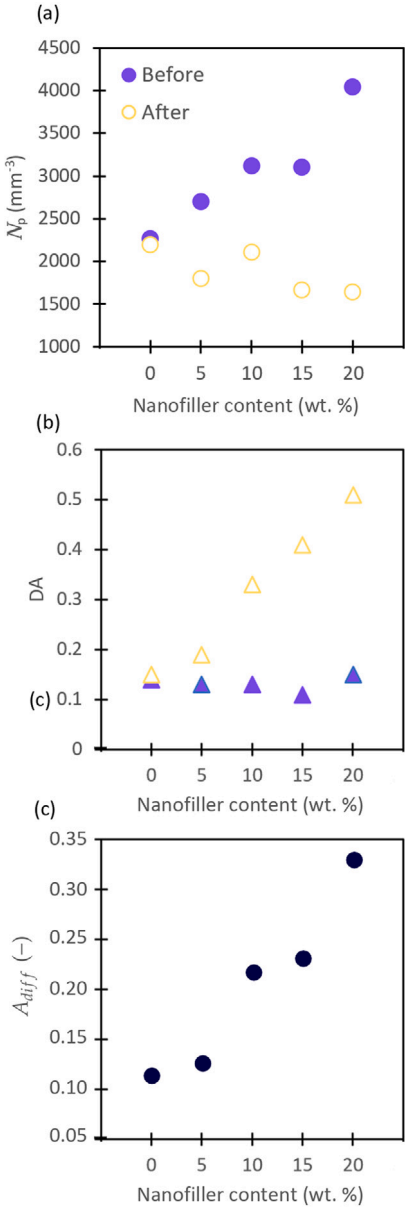

Fig. 7. Evolution of the number of pores N_p (a) and the degree of anisotropy DA (b) before and after (one day of recovery time) fatigue tests as function of the nanofiller content. Difference A_{diff} between the 3D mean curvature distributions before and after (one day of recovery time) fatigue tests as function of the nanofiller content (c).

3.4. Design of filled EVA foams for energy absorption applications: the case of running shoes

EVA foams are widely used as lightweight, soft and superelastic architectured materials for packaging, automotive and sport structures or systems to mention a few application domains. Hence, the design of these foams often involves a complex trade off between lightweight, absorption and dissipation of mechanical loadings throughout their entire usage phase. Among the standard design criteria, durability thus becomes another key performance criterion, in particular for foams subjected to many and repeated loadings. This is typically the case for EVA foams used in running shoe midsoles, which must be engineered to balance minimal density and optimal cushioning with superior rebound properties and restrained mechanical aging. The fatigue data we report in this study can provide some helpful information towards the design

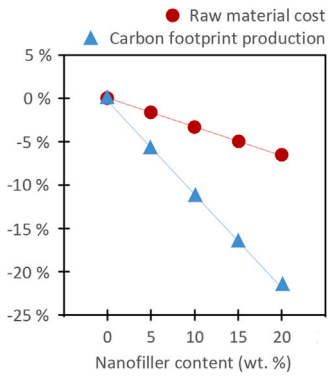

Fig. 8. Evolution of the cost and environmental footprint of production of the studied EVA foams filled with silica nanoparticles extracted from rice husk ash.

of these foams when they are filled with the selected biosourced nanoparticles:

- The foam specific properties are enhanced both initially and throughout fatigue with the nanofiller content, making the midsole more lightweight.
- Meanwhile, increasing the nanofiller content fastens the degradation kinetics of mechanical properties during fatigue.
- Although the cushioning properties of filled foams are initially worse than unfilled foams, they become practically equally effective during fatigue.
- The incorporation of such fillers reduces the rebound properties of the foam, before and after fatigue as nanofilled foams dissipate more energy during a cycle.

The foam design is also motivated both by the production cost and the environmental footprint. We estimated the cost and the environmental impacts associated with the incorporation of biosourced silica into the different EVA foams using a partial life cycle assessment which focuses exclusively on the raw materials and related foams productions. This approach follows the requirements and recommendations of the standards [33] and the Product Environmental Footprint (PEF) method [34]. The details of the calculation are given in Appendix. As illustrated in Fig. 8, both the cost and the environmental footprint related to the production of the studied EVA foams (and their raw materials) decrease linearly with the nanofiller content down to 6 % and 21 %, respectively.

Thus, a proper balance in functional properties – lightness, cushioning, rebound and durability – and the industrial strategic interest – including the cost and the carbon footprint reductions of the foam production – should be achieved with nanofiller contents around 10 wt.%. Such a choice should allow the design of durable EVA midsoles with (i) enhanced lightness ($\approx 30-40$ %) while maintaining good cushioning properties with acceptable decrease of rebound properties ($\approx 20-30$ %), (ii) decreased cost (≈ 2.5%) as well as carbon footprint (≈ 12 %) of the foam production.

4. Conclusion

This study examined the influence of biosourced silica content on the compression fatigue behavior of closed-cell EVA foams, with a specific focus on the microstructural changes induced by cyclic loading. By maintaining constant porosity across all materials, the intrinsic effect of nanofiller content could be isolated from porosity-related effects.

At the macroscopic scale, increasing filler content resulted in higher initial stiffness, stress levels and absorbed energy under compression, together with significant changes in fatigue behavior and strain recovery. While low to moderate filler contents improved resistance to cyclic deformation, higher contents promoted irreversible deformation and accelerated degradation under long-term cyclic loading, revealing a trade-off between (a) mechanical reinforcement, (b) cushioning and rebound properties and (c) fatigue durability.

Post-compression microstructural analyses showed that cyclic loading induces pronounced, filler-dependent modifications of cell wall morphology, including bending and localized tears of cell walls. These deformation-induced morphological features should not be regarded as independent design parameters, but rather as microstructural signatures of the underlying deformation and damage mechanisms activated during compression fatigue.

Overall, the present results demonstrate that filler content governs the compression fatigue performance of biosourced silica-reinforced EVA foams primarily through its influence on the evolution of deformation-induced cellular morphology. By combining controlled formulation, mechanical testing and three-dimensional post-deformation characterization, this work provides mechanistic insights and practical guidance for selecting filler content in the design of lightweight and durable energy-absorbing EVA foams.

CRediT authorship contribution statement

C. Aimar: Writing – original draft, Visualization, Methodology, Investigation. **R. Bordage:** Visualization, Investigation. **D. Ferré Sentis:** Writing – review & editing, Supervision, Methodology, Conceptualization. **L. Bailly:** Writing – review & editing, Supervision, Methodology, Conceptualization. **S. Rolland du Roscoat:** Writing – review & editing, Supervision, Methodology, Conceptualization. **A. Kayum:** Resources, Investigation. **L. Orgéas:** Writing – review & editing, Validation, Supervision, Project administration, Methodology, Funding acquisition, Conceptualization.

Declaration of competing interest

The authors declare the following financial interests/personal relationships which may be considered as potential competing interests: Clara Aimar reports financial support was provided by Association Nationale Recherche Technologie. If the other authors declare that they have no known competing financial interests or personal relationships that could have appeared to influence the work reported in this paper.

Acknowledgments

Olga Stamati, Frédéric Charlot and Erwan Chabert are gratefully acknowledged for their technical assistance, Luca Marcello for his insightful advice regarding the life cycle assessment. This research has also benefited from the characterization equipment of the Grenoble INP – CMTC. C. Aimar thanks Decathlon and ANRT (grant 2019/1038) for their sponsorship. This work was carried out within the Laboratoire Sols Solides Structures Risques, a member of Tec 21 (ANR-11-LABX-0030) and PolyNat (ANR16-CARN-0025).

Appendix. Estimation of the cost and environmental footprint of foam production

The definition of the study goal and scope follows a cradle-to-gate approach, limited to the extraction, processing, and production of transformed materials, without considering transportation and industrial compounding or any other manufacturing process, which were deemed non-differentiating for this initial analysis.

The functional unit is one kilogram of masterbatch, enabling a standardized comparison of different incorporation scenarios. The life cycle inventory relies on generic data exclusively sourced from the EF 3.1 database. The only exceptions are the data for biosourced silica and DCP which are derived from a semi-specific inventory combining primary data from one of Decathlon's suppliers and secondary data

from EF 3.1. This modeling undergoes an external peer review and fully complies with the PEF method.

The impact assessment was conducted using the EF 3.1 method, with a focus on the climate change midpoint indicator and the endpoint EF single score. The results must be interpreted considering the quality and representativeness of the inventory data and the exclusion of certain life cycle stages, which may influence the extent of the observed environmental benefits.

Data availability

Data will be made available on request.

References

[1] R. Verdejo, N.J. Mills, Performance of EVA foam in running shoes, in: The Engineering of Sport, vol. 4, Blackwell Science, 2002, pp. 580–588.

[2] T. Allen, M. Pagan, R. Martin, O. Duncan, Effect of rest periods on mechanical ageing of running shoes, Proc. Multidiscip. Digit. Publ. Inst. 49 (1) (2020) 138, http://dx.doi.org/10.3390/proceedings2020049138.

[3] N. Lippa, D. Krzeminski, S. Piland, J. Rawlins, T. Gould, Biofidelic mechanical ageing of ethylene vinyl acetate running footwear midsole foam, Proc. Inst. Mech. Eng. Part P: J. Sport. Eng. Technol. 231 (2016) http://dx.doi.org/10.1177/1754337116678153.

[4] Y. Shimazaki, S. Nozu, T. Inoue, Shock-absorption properties of functionally graded EVA laminates for footwear design, Polym. Test. 54 (2016) 98–103, http://dx.doi.org/10.1016/j.polymertesting.2016.04.024.

[5] X. Sun, W.K. Lam, X. Zhang, J. Wang, W. Fu, Systematic review of the role of footwear constructions in running biomechanics: Implications for running-related injury and performance, J. Sport. Sci. Med. 19 (1) (2020) 20–37.

[6] C. Aimar, L. Orgéas, S. Rolland du Roscoat, L. Bailly, D. Ferré Sentis, Compression fatigue of elastomeric foams used in midsoles of running shoes, Footwear Sci. 16 (2024) 1–11, http://dx.doi.org/10.1080/19424280.2024.2317881.

[7] J. Zhang, V. Hirschberg, D. Rodrigue, Mechanical fatigue of polymer foams - a review, Polym. Rev. 63 (4) (2023) 866–894, http://dx.doi.org/10.1080/15583724.2023.2228874.

[8] B.B. Boonstra, Role of particulate fillers in elastomer reinforcement: a review, Polymer 20 (6) (1979) 691–704, http://dx.doi.org/10.1016/0032-3861(79)90243-X.

[9] S.T. Lee, C.B. Park, Foam Extrusion: Principles and Practice, second ed., in: Polymeric Foams, 2014.

[10] B.P. Chang, A. Kashcheev, A. Veksha, G. Lisak, R. Goei, K.F. Leong, et al., Nanocomposite foams with balanced mechanical properties and energy return from EVA and CNT for the midsole of sports footwear application, Polymers 15 (4) (2023) 948, http://dx.doi.org/10.3390/polym15040948.

[11] B. Dong, C. Liu, Y. Wu, Fracture and fatigue of silica-carbon black-natural rubber composites, Polym. Test. 38 (2014) 40–45, http://dx.doi.org/10.1016/j.polymertesting.2014.06.004.

[12] A. Menon, C. Pillai, W. Jin, C. Nah, Fatigue resistance of silica-filled natural rubber vulcanizates: Comparative study of the effect of phosphorylated cardanol prepolymer and a silane coupling agent, Polym. Int. 54 (2005) 629–635, http://dx.doi.org/10.1002/pi.1720.

[13] J. Payá, J. Monzó, M.V. Borrachero, A. Mellado, L.M. Ordoñez, Determination of amorphous silica in rice husk ash by a rapid analytical method, Cem. Concr. Res. 31 (2) (2001) 227–231, http://dx.doi.org/10.1016/S0008-8846(00)00466-X.

[14] T.H. Liou, Preparation and characterization of nano-structured silica from rice husk, Mater. Sci. Eng.: A 364 (1) (2004) 313–323, http://dx.doi.org/10.1016/j.msea.2003.08.045.

[15] H.M. Da Costa, L.L.Y. Visconte, R.C.R. Nunes, C.R.G. Furtado, Mechanical and dynamic mechanical properties of rice husk ash–filled natural rubber compounds, J. Appl. Polym. Sci. 83 (11) (2002) 2331–2346, http://dx.doi.org/10.1002/app.10125.

[16] A.S.S. Singaravelu, J.J. Williams, J. Ruppert, M. Henderson, C. Holmes, N. Chawla, In situ x-ray microtomography of the compression behaviour of eTPU bead foams with a unique graded structure, J. Mater. Sci. 56 (8) (2020) 5082–5099, http://dx.doi.org/10.1007/s10853-020-05621-3.

[17] R. Verdejo, N.J. Mills, Heel—shoe interactions and the durability of EVA foam running-shoe midsoles, J. Biomech. 37 (9) (2004) 1379–1386, http://dx.doi.org/10.1016/j.jbiomech.2003.12.022.

[18] C. Aimar, L. Orgéas, S. Rolland du Roscoat, L. Bailly, D. Ferré Sentis, Fatigue mechanisms of a closed cell elastomeric foam: A mechanical and microstructural study using ex situ x-ray microtomography, Polym. Test. 128 (2023) 108194, http://dx.doi.org/10.1016/j.polymertesting.2023.108194.

[19] M.S.M. Basri, F. Mustapha, N. Mazlan, M.R. Ishak, Optimization of rice husk ash-based geopolymers coating composite for enhancement in flexural properties and microstructure using response surface methodology, Coatings 10 (2020) 165, http://dx.doi.org/10.3390/coatings10020165.

[20] E. Ayswarya, K. Vidya Francis, V. Renju, E.T. Thachil, Rice husk ash: A valuable reinforcement for high density polyethylene, Mater. Des. 41 (2012) 1–7, http://dx.doi.org/10.1016/j.matdes.2012.04.035.

[21] O. Stamati, E. Andò, E. Roubin, R. Cailletaud, M. Wiebicke, G. Pinzon, et al., 'Spam': Software for practical analysis of materials, J. Open Source Softw. 5 (51) (2020) 2286, http://dx.doi.org/10.21105/joss.02286.

[22] J. Schindelin, I. Arganda-Carreras, E. Frise, V. Kaynig, M. Longair, T. Pietzsch, et al., Fiji: an open-source platform for biological-image analysis, Nature Methods 9 (7) (2012) 676–682, http://dx.doi.org/10.1038/nmeth.2019.

[23] I. Arganda-Carreras, V. Kaynig, C. Rueden, K.W. Eliceiri, J. Schindelin, A. Cardona, et al., Trainable weka segmentation: a machine learning tool for microscopy pixel classification, Bioinformatics 33 (15) (2017) 2424–2426, http://dx.doi.org/10.1093/bioinformatics/btx180.

[24] V. Boulos, L. Salvo, V. Fristot, P. Lhuissier, D. Houzet, Investigating performance variations of an optimized gpu-ported granulometry algorithm, in: Proceedings of the Conference on Design and Architectures for Signal and Image Processing, DASIP, Karlsruhe, Germany, 2012, pp. 1–6, URL: https://hal.science/hal-00787861.

[25] M. Doube, M.M. Kłosowski, I. Arganda-Carreras, F. Cordelières, R. Dougherty, J.S. Jackson, et al., BoneJ: Free and extensible bone image analysis in ImageJ, Bone 47 (6) (2010) 1076–1079, http://dx.doi.org/10.1016/j.bone.2010.08.023.

[26] R. Verdejo, N.J. Mills, Simulating the effects of long distance running on shoe midsole foam, Polym. Test. 23 (5) (2004) 567–574, http://dx.doi.org/10.1016/j.polymertesting.2003.11.005.

[27] S. Machado, V. Mercier, N. Chiaruttini, LimeSeg: a coarse-grained lipid membrane simulation for 3d image segmentation, BMC Bioinform. 20 (1) (2019) 2, http://dx.doi.org/10.1186/s12859-018-2471-0.

[28] K. Brückner, S. Odenwald, S. Schwanitz, J. Heidenfelder, T. Milani, Polyurethane-foam midsoles in running shoes - impact energy and damping, Procedia Eng. 2 (2) (2010) 2789–2793, http://dx.doi.org/10.1016/j.proeng.2010.04.067.

[29] S. Pardo-Alonso, E. Solórzano, S. Estravís, M.A. Rodríguez-Perez, J.A.d. Saja, In situ evidence of the nanoparticle nucleating effect in polyure- thane nanoclay foamed systems, Soft Matter 8 (44) (2012) 11262–11270, http://dx.doi.org/10.1039/C2SM25983D.

[30] S. Pardo-Alonso, E. Solórzano, L. Brabant, P. Vanderniepen, M. Dierick, L. Van Hoorebeke, et al., 3D analysis of the progressive modification of the cellular architecture in polyureth ane nanocomposite foams via x-ray microtomography, Eur. Polym. J. 49 (5) (2013) 999–1006, http://dx.doi.org/10.1016/j.eurpolymj.2013.01.005.

[31] I.J. Gibson, M.F. Ashby, The mechanics of three-dimensional cellular materials, Proc. R. Soc. A (1782) (1982) 43–59, http://dx.doi.org/10.1098/rspa.1982.0088.

[32] L.J. Gibson, M.F. Ashby, Cellular Solids: Structure and Properties, Cambridge University Press, 1999, http://dx.doi.org/10.1017/CBO9781139878326.

[33] ISO 14040, Environmental Management – Life Cycle Assessment – Principles and Framework, Tech. Rep., International Organization for Standardization, Geneva, Switzerland, 2006.

[34] European Commission, Directorate-General for Environment, Environmental Footprint Methods – Benefits for Companies – Overview of the Environmental Footprint Methods, Tech. Rep., Publications Office of the European Union Union, Luxembourg, 2024, http://dx.doi.org/10.2779/8944075.